Princeton Plasma Physics Laboratory

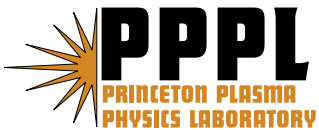## Magnetic Energy Release
during the 2002 September 9 Solar Flare

Jeongwoo Lee, Dale E. Gary,
and G.S. Choe

November 2006

Princeton Plasma Physics Laboratory
Report Disclaimers

Full Legal Disclaimer

This report was prepared as an account of work sponsored by an agency of the United States Government. Neither the United States Government nor any agency thereof, nor any of their employees, nor any of their contractors, subcontractors or their employees, makes any warranty, express or implied, or assumes any legal liability or responsibility for the accuracy, completeness, or any third party's use or the results of such use of any information, apparatus, product, or process disclosed, or represents that its use would not infringe privately owned rights. Reference herein to any specific commercial product, process, or service by trade name, trademark, manufacturer, or otherwise, does not necessarily constitute or imply its endorsement, recommendation, or favoring by the United States Government or any agency thereof or its contractors or subcontractors. The views and opinions of authors expressed herein do not necessarily state or reflect those of the United States Government or any agency thereof.

Trademark Disclaimer

Reference herein to any specific commercial product, process, or service by trade name, trademark, manufacturer, or otherwise, does not necessarily constitute or imply its endorsement, recommendation, or favoring by the United States Government or any agency thereof or its contractors or subcontractors.

PPPL Report Availability

Princeton Plasma Physics Laboratory:

http://www.pppl.gov/pub_report/

Office of Scientific and Technical Information (OSTI):

http://www.osti.gov/bridge

U.S. Department of Energy:

U.S. Department of Energy
Office of Scientific and Technical Information
P.O. Box 62
Oak Ridge, TN 37831-0062
Telephone: (865) 576-8401
Fax: (865) 576-5728
E-mail: reports@adonis.osti.gov

MAGNETIC ENERGY RELEASE DURING THE 2002 SEPTEMBER 9 SOLAR FLARE

Jeongwoo Lee,[1] Dale E. Gary,[1] and G. S. Choe[2]

ABSTRACT

We study the magnetic energy release during the 2002 September 9 flare using the high-cadence (40 ms) Hα filtergram at Big Bear Solar Observatory (BBSO), along with hard X-ray and microwave data from the *Reuven Ramaty High-Energy Solar Spectroscopic Imager* (*RHESSI*) and the Owens Valley Solar Array (OVSA), respectively. We take the Poynting vector approach with the standard two-dimensional geometry of the reconnecting current sheet (RCS) but suggest a new technique to infer the area of the RCS, in order to complete the magnetic energy calculation entirely with observed quantities. We found five peaks of impulsive magnetic energy release, concentrated within 10–30 s periods, that are episodic with the peaks of the hard X-ray light curve. The maximum amount of energy released per peak reaches $\sim 2.6 \times 10^{30}$ ergs s^{-1}, and the electron energy deposition rate derived from the *RHESSI* spectra falls into the range of 10%–80% of the magnetic energy release rate. We briefly discuss this result in comparison with other studies thus far made toward understanding of the magnetic reconnection in solar flares and suggest the pulsating current sheet model as the most plausible interpretation of our result.

Subject headings: Sun: flares — Sun: magnetic fields — Sun: particle emission

Online material: color figure

1. INTRODUCTION

Under the general model that solar flares are mainly powered by magnetic reconnection, any observable quantities associated with the magnetic reconnection process will help to advance the understanding of solar flare physics. Much studied in this regard is the relationship first suggested by Forbes & Priest (1982, hereafter FP82) linking the spread of Hα kernels in two-ribbon flares with the electric field in the reconnecting current sheet (RCS) above the newly forming loop system. Upon integration of the electric field over the ribbon length, we can further determine the electric potential drop or, equivalently, the rate of reconnecting magnetic flux as an important measure for both magnetic reconnection and particle acceleration (Priest & Forbes 2000, 2002). These theoretical ideas opened a new area of study in which the flux reconnection rate derived from ribbon motion is compared with the timing of hard X-ray and microwave emissions, and the result often provides qualitative support for magnetic reconnection as the flare driver on the basis of a similarity of time profiles (e.g., Fletcher & Hudson 2001, 2002; Asai et al. 2002, 2004a; Qiu et al. 2002; Jing et al. 2005; Isobe et al. 2002, 2005; Noglik et al. 2005).

While the above interpretation of the two-ribbon flares has generally been accepted, an alternative view was recently raised by Grigis & Benz (2005), who presented an event of X-ray footpoints moving parallel to the neutral line, as opposed to the FP82 model. In such cases the key relationship between the observed ribbon velocity and the magnetic reconnection rate as predicted by the FP82 model is inapplicable, even though the X-ray flux and footpoint motion appear to be correlated in time with each other. In an earlier study by Asai et al. (2004a) it was also pointed out that actual ribbon motion may have velocity components both perpendicular and parallel to the magnetic neutral line and that only the perpendicular velocity com-

ponent should be used in calculating the flux reconnecting rate to keep consistency with the model. The directivity of the ribbon motion relative to ambient magnetic field is thus an important criterion for applying the FP82 model to observations of ribbon separation.

Within the FP82 model, another important quantity for the reconnection process is the Poynting vector at the RCS (e.g., Priest 1982). Since the Poynting vector signifies total magnetic energy flux density, its product with the area of the RCS provides the magnetic energy release rate in the RCS. To our knowledge, Isobe et al. (2002) made the first attempt to use the Poynting flux in an analysis of solar flare data to calculate the magnetic energy release, and Asai et al. (2002, 2004a) and Isobe et al. (2005) have continued to apply the technique to solar flare observations. More recently, Krucker et al. (2005) compared such magnetic energy with the electron energy deposition rate derived from a hard X-ray spectrum for agreement. As illustrated by these studies, the release rate of magnetic energy is highly relevant to the interpretation of various types of flare-associated radiation, since it can be directly compared with the energy of radiating particles. Such comparisons can test the hypothesis that a certain portion of the magnetic energy is imparted to the particle energy during solar flares (Lin et al. 2002). The electric voltage in the RCS, which is the main quantity predicted by the FP82 model, also represents a source of energy. However, the voltage is more relevant than the total energy to the efficiency of energization per particle under the DC field acceleration mechanism (e.g., Litvinenko 2000). Unlike the electric field, calculation of the energy release rate requires two additional parameters that cannot be directly observed—the lateral area of the RCS and the ambient magnetic field in the RCS—for which simplifying assumptions must be made (see, e.g., Asai et al. 2004a).

In this paper we make a more quantitative, although empirical, approach to the determination of the magnetic energy by making use of the ribbon area observed on the surface. The ribbon area will not be a significant quantity if the diffusion region is really pointlike in two dimensions (or linelike in 2.5 dimensions). But if the RCS has a finite area, as it must in reality, its counterpart at

[1] Physics Department, New Jersey Institute of Technology, 161 Warren Street, Newark, NJ 07102.

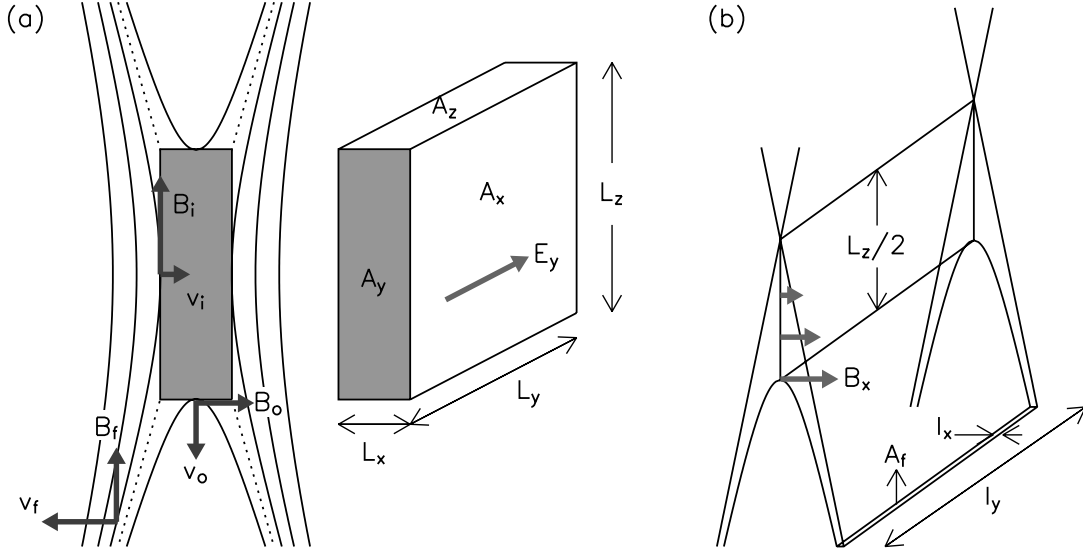[2] Princeton Plasma Physics Laboratory, Princeton University, Princeton, NJ 08543.

FIG. 1.—Schematic plots of the magnetic field configurations around the RCS. (*a*) Electromagnetic field, velocity, and area vectors (*thick arrows*) and the lengths of the sides of the RCS (*thin arrows*). The shaded region represents the cross section of the RCS in the *x-z* plane, and the dotted lines are the separatrices. The subscripts *i*, *o*, and *f* represent the incoming, outgoing, and footpoint field lines, respectively. (*b*) RCS and flare ribbon shown together to illustrate their relationship. The ribbon area is $A_f \equiv l_x l_y$, and the RCS area pointing to the *x*-axis is $A_x \equiv L_y L_z = l_y L_z$.

the solar surface will most likely be the area of that part of the ribbon to which it is connected and can, in combination with the Poynting vector, be a critical factor in determining the magnitude of the magnetic energy release rate. We investigate how that instantaneously reconnecting part of the ribbon can be identified observationally. We start by refining the theoretical picture of magnetic reconnection in § 2 and present observational data in § 3. After identifying the instantaneously reconnecting part of the ribbon, we determine the magnetic energy release rate and electron energy in § 4. The physical implication of the result is discussed in § 5.

2. THEORETICAL BACKGROUND

We briefly introduce in this section the FP82 model (see also Priest & Forbes 2002) and describe how we make use of the model to determine the energy release rate. Figure 1 shows the magnetic field configuration and other physical parameters around the RCS. In Figure 1*a*, the separatrices are shown as dotted lines and the RCS as the shaded slab centered at the X-point. The vectors A, E, and B represent the area, electric, and magnetic fields in the RCS, respectively, used along with subscripts: *i* for incoming fields, *o* for outgoing fields, and *f* for the footpoint fields. In this configuration, $(\boldsymbol{B}_o, \boldsymbol{v}_i, \boldsymbol{v}_f)$ have only an *x*-component while $(\boldsymbol{B}_i, \boldsymbol{B}_f, \boldsymbol{v}_o)$ have only a *z*-component, and, for simplicity, we drop the vector component notations for these quantities. The Poynting flux coming from one side is $\boldsymbol{S}_i = (c/4\pi)(\boldsymbol{E}_i \times \boldsymbol{B}_i) = (cE_yB_i/4\pi)\hat{\boldsymbol{x}}$, where *c* is the speed of light. The total electromagnetic energy change solely due to the Poynting fluxes coming from both sides into the RCS is then expressed by

$$-\frac{\partial \mathcal{E}_B}{\partial t} = 2\boldsymbol{S}_i \cdot \boldsymbol{A}_x = \frac{c}{2\pi}\left(E_y B_i A_x\right). \quad (1)$$

To claim this quantity as the energy release rate in the RCS, we assume that most of the incoming energy flux ($S_x A_x$) is consumed inside the RCS and the outgoing energy flux ($S_z A_z$) carries a negligible amount of energy. We show in the Appendix that this approximation holds when the reconnection is efficient, as is commonly assumed for solar flares. The FP82 model itself gives only the relationship between the electric field and footpoint motion,

$$E_y = \frac{v_i B_i}{c} = \frac{v_f B_f}{c}, \quad (2)$$

and the flux change rate defined by $\dot{\Phi}_B = E_y l_y$. We are thus left with only two unknown variables: B_i and A_x in equation (1). This is the point at which further assumptions are made. For instance, Isobe et al. (2002, 2005) used the size of an arcade for the area A_x, while Asai et al. (2004a) used the coronal field extrapolation technique to infer B_i from B_f.

The refinement that we make here is to relate the unknown quantity $A_x B_i$ to the flux measured at the footpoint, $A_f B_f$, under the flux conservation law and the geometry of the RCS. Before constructing such a relationship, we note that the second equality in equation (2) is also based on the flux conservation law, and we need to clarify how our approach reconciles with the standard model. Equation (2) is asymptotically valid in the limit of infinitely thin RCS (i.e., $L_x \approx 0$) because the incoming field lines are those *not yet* reconnected, whereas the footpoint emission occurs just *after* the reconnection. Since the field lines stemming from the ribbon A_f are, in fact, those engaged in instantaneous reconnection, they (whose strength through A_x is denoted B_x) would pass through the lower half of A_x as shown in Figure 1*b*. Our proposal is that the flux conservation law can be applied not only to the incoming B_z-component (as in eq. [2]) but to the outgoing B_x-component in the RCS. Namely, the magnetic flux through A_f equals the flux going through A_x as

$$\int_0^{L_z/2} B_x L_y \, dz = B_f A_f. \quad (3)$$

The strength of B_x in this expression will vary from $B_x = B_o$ at the bottom of the RCS to $B_x = 0$ at the X-point. Assuming a linear variation of B_x across L_z, we reduce equation (3) to $A_x B_o = 4 B_f A_f$. What we need to know to close this calculation is therefore a relationship between B_o and B_i. To go back to the RCS geometry shown in Figure 1*a*, this ratio is, in fact, simply the

aspect ratio of the RCS, which, in turn, corresponds to the definition of the reconnection rate, M (Petschek 1964):

$$M \equiv \frac{L_x}{L_z} = \left|\frac{B_o}{B_i}\right| < 1. \tag{4}$$

In this study, we use $M \approx 0.1$, based on a numerical experiment of the Petschek model (Yan et al. 1992). Under these considerations, we replace equation (1) with

$$\frac{\partial \mathcal{E}_{em}}{\partial t} = -\frac{2\left|v_f B_f^2 A_f\right|}{\pi M}, \tag{5}$$

which can entirely be determined by the observables. This expression, aside from the numerical factor, might be mistaken as some change in the magnetic energy density and volume in the footpoint. This is, however, only an apparent form. For instance, v_f in equations (2) and (5) does not stand for the actual motion of footpoint magnetic field lines, and the quantities in the right-hand side of equation (5) represent only the change in the footpoint features associated with the actual energy change in the coronal RCS.

It is worthwhile to briefly mention a couple of issues that need to be addressed observationally prior to using these equations. First, as a general remark, we note that the FP82 model requires the two-dimensional symmetry to enable the analytic expression for the electric field (eq. [2]). In reality, we believe that these equations can be used approximately as far as the region of interest is found topologically equivalent to the two-dimensional model. Second, in using equation (5), note that flare ribbons in the Hα center line correspond not only to the instantaneously reconnecting area A_f but also to already reconnected field lines in the newly formed, closed arcade, by virtue of Hα's slow decay in brightness. To measure the area A_f, we need a type of radiation that is sensitive to energetic particles but cools rapidly once the precipitating particles cease, so that its flare kernel shows only the instantaneously reconnected area. Third, the velocity v_f should be properly defined taking into account the finite size of the ribbon area because in this paradigm, any type of time-dependent change in area can occur independent of the velocity perpendicular to its length. Fourth, the unknown filling factor problem is frequently mentioned as leading to a possible underestimation of the true magnetic field. However, we believe that the present technique is insensitive to the filling factor because both $B_i A_x$ and $v_i B_i$ are integral quantities obeying the magnetic flux conservation law. Finally, we consider time cadence rather important as insufficient time resolution can lead to underestimation of the ribbon speed and consequently to the electric field and energy release rate. A cadence commensurate with the spatial resolution and the speed of the ribbon motion is therefore desirable.

3. OBSERVATION

The 2002 September 9 flare occurred in NOAA AR 0105 and GOES (Geostationary Operational Environmental Satellite) soft X-ray class M2.3. We select this event mainly because it has been observed with Hα filtergrams at an unusually high cadence (40 ms) at Big Bear Solar Observatory (BBSO), which we find is essential for the goal of this study. We also use hard X-ray data from the Reuven Ramaty High-Energy Solar Spectroscopic Imager (RHESSI) and microwave data from the Owens Valley Solar Array (OVSA) to gather information on the high-energy electrons.

3.1. The BBSO Hα Data

The BBSO Hα line-center data consist of full-disk images with a 1 minute time cadence and the blue-wing (-1.3 Å) partial-frame images at high cadence (40 ms) and high spatial resolution ($0\rlap{.}''87$ pixel^{-1}). The high-cadence images are important for accurate determination of the ribbon speed, but perhaps more important is the off-band property of the images. Since brightening of the chromosphere at the Hα blue wing requires more energetic particles than at the line center, we expect that the ribbon area observed in off-band Hα would be a better proxy for the instantaneously reconnecting area than Hα center-line images would provide. To what extent it is a proxy could be studied by theoretical modeling of the Hα line profiles under nonthermal electron heating (e.g., Canfield et al. 1984), which is beyond the scope of this paper. Here we argue in favor of off-band Hα based simply on the appearance of the images at the center line and off-band.

Figure 2 (left) shows an Hα blue-wing image as contours and the line-center image as a gray-scale image observed at the same time. We can see that the Hα -1.3 Å kernels are smaller in size than the Hα center-line ribbons and are located at their leading edge. This morphology suggests that the area heated by the instantaneously precipitating particles is confined to the leading edge of the Hα line-center ribbons and is better represented by the blue-wing images. The relatively smaller area of the ribbon at the blue wing by no means guarantees that it exactly represents the instantaneous region of energetic particle precipitation. We thus further examine the one-dimensional profiles of the center-line and off-band intensities in Figure 2 (right). It appears that the intensity distribution across the Hα blue-wing ribbon (thin line) is more or less symmetric, whereas that at center line (thick line) is asymmetric, with a broad tail to the left in the figure. Since the Hα center-line intensity is more easily enhanced, the asymmetric intensity distribution across the center-line ribbon implies that the chromospheric area instantaneously connected to the coronal energy release is confined only to the leading edge, and the trailing part includes the previously heated area. Since the off-band ribbon is both symmetric and confined to the leading edge of the center-line ribbon, we can regard this as a proxy for the area affected most strongly at any instant. The Hα off-band data are therefore important to this study for their sensitivity to the presence of more energetic electrons.

In principle, off-band Hα in either the red or the blue wing may be useful for identifying the instantaneously reconnecting area, but we note that a red-wing asymmetry is observed to be much more common in flares (Tang 1983) and is interpreted as due to downward Doppler shifts associated with reconnection flow (e.g., Asai et al. 2004b). This suggests that blue-wing Hα is superior to red-wing Hα as a proxy of energetic particle precipitation, being less affected by bulk motions.

3.2. The RHESSI Hard X-Ray Data

Hard X-rays are due to bremsstrahlung of high-energy electrons, most often those precipitating into the chromosphere (Dennis 1988), and can therefore be ideal for studying the footpoint motions associated with the primary energy release. In the 2002 September 9 event, however, the hard X-ray emission appears to span the region between Hα ribbons and hence is dominated by a loop source. Figure 3 shows an X-ray map superimposed on an Hα blue-wing (-1.3 Å) image at 17:45:50 UT in the middle of the flare. Three Hα ribbons, denoted $a1$, $a2$, and b, respectively, are named following the same convention as used by Ji et al. (2004), who studied this event in detail. The X-ray
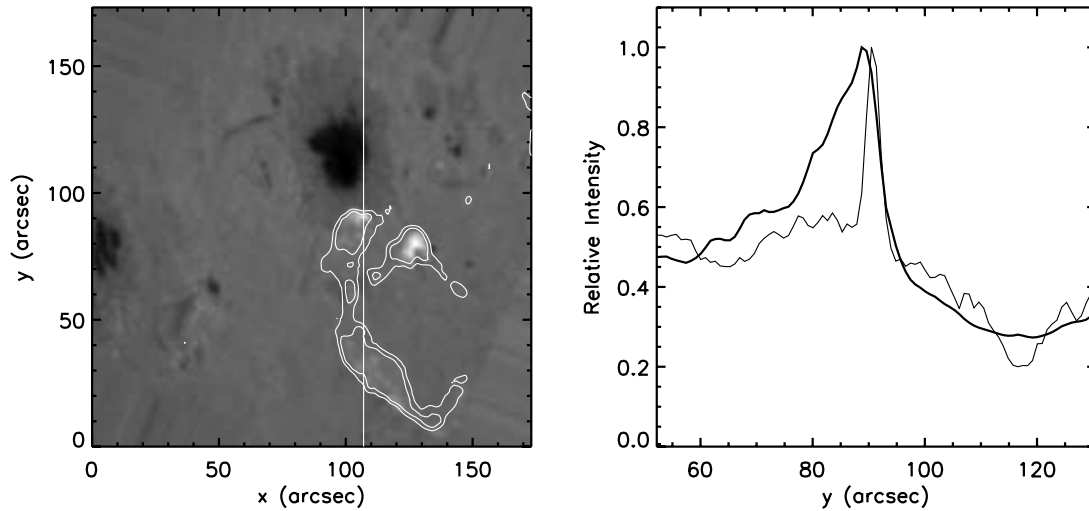
Fig. 2.—Flare ribbons at Hα line center and blue wing. *Left*: Hα −1.3 Å (*contours*) plotted over the Hα line-center image (*gray scale*). *Right*: One-dimensional profiles of the Hα −1.3 Å (*thin line*) and line-center emission (*thick line*). The blue-wing ribbon emission appears much narrower and is confined to the leading edge of the line-center ribbon and thus is regarded as representing the instantaneously reconnecting area in the chromosphere. The Hα center-line image was taken at 17:50:25 UT and the blue-wing image at 17:50:25.023 UT.

map (*contours*) is created using the CLEAN method from *RHESSI* data in the 25−50 keV range and appears as a single source lying between the Hα kernels, implying a single loop system in which the hard X-ray source sits at the loop top. While we showed in Figure 3 the *RHESSI* map only at one time, Ji et al. (2004) presented a more detailed imaging of this *RHESSI* source using the PIXON method at multiple times throughout the flare in search of any footpoint source. In their result, too, the morphology changes only a little with time and energy, and most of the hard X-ray flux comes from the loop top at all times.

We thus decide to use the hard X-ray light curves mainly as a good indicator of the primary energy release at the loop top.

The three right panels in Figure 3 show the 25−50 keV light curve (*top*) and time derivatives of the Hα light curves from the *a*1 and *a*2 kernels (*middle*) and from kernel *b* (*bottom*). Comparison of spatially resolved light curves like these may allow the inference of magnetic connections between the spatially distinct radiative sources. We plot the time derivative of the Hα light curve rather than the original light curve because the former shows more obvious correlation with the X-ray light
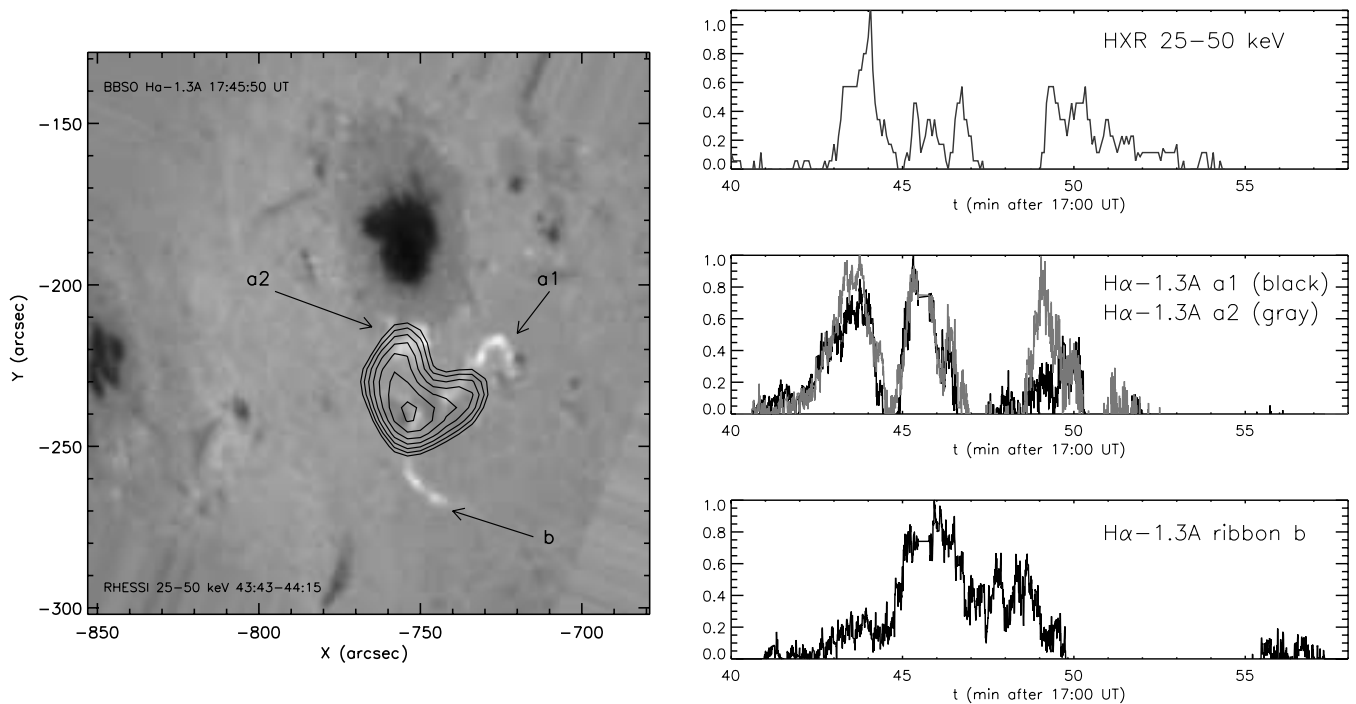

Fig. 3.—Hard X-ray map and light curves in comparison with Hα data. *Left*: *RHESSI* map at 25−50 keV (*contours*) on top of a BBSO Hα blue-wing image (*gray scale*) near the flare peak time (17:45:50 UT). The hard X-ray 25−50 keV emission appears as a simple, static source between the Hα blue-wing kernels. It can be identified as a loop source. *Top right*: Hard X-ray light curve at 25−50 keV. *Middle and bottom right*: Time derivative of the Hα blue-wing −1.3 Å light curves at ribbon *a*1 (*black line*) and *a*2 (*gray line*), and at ribbon *b*, respectively. The Hα light curves are excess intensities normalized to the peak value and integrated over individual ribbons.
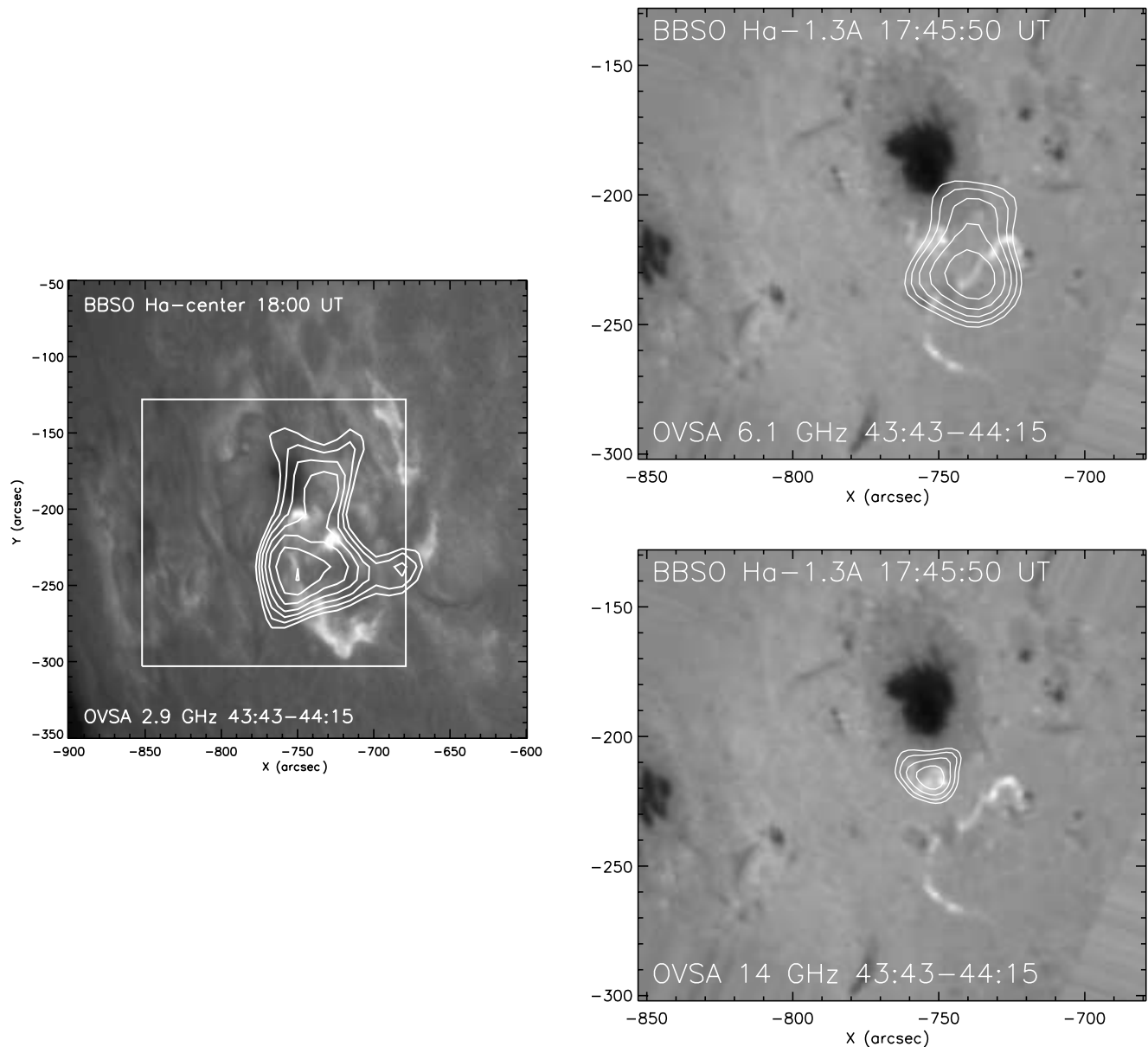
Fig. 4.—Microwave maps at three frequencies, 2.9, 6.1, and 14.0 GHz, as contours at 17:43 UT. The 2.9 GHz map is plotted over an Hα center-line image with a larger field of view, and the 6.0 and 14 GHz maps are shown over the off-band images. The white box in the left panel indicates the area selected for display in the right panels. [*See the electronic edition of the Journal for a color version of this figure.*]

curve (cf. Dennis et al. 2003). The differential light curves from *a*1 and *a*2 almost perfectly coincide with the X-ray light curve, whereas that of ribbon *b* shows only one peak (centered at 17:46 UT) matching its X-ray counterpart. The agreement between the *a*1 and *a*2 light curves and the X-ray light curve supports the above speculation that the X-ray source is at the loop top between two Hα conjugate footpoints. The differential light curve of ribbon *b* implies that this ribbon formed by an intense particle precipitation at ∼17:46 UT and stretches out to the southwest. What is important for the goal of this study is the motion of the ribbons corresponding to the multiple peaks in the light curve at 25–50 keV, which we check with the microwave data.

3.3. *The OVSA Microwave Data*

Figure 4 shows the microwave maps obtained with OVSA at three frequencies at a single time, 17:43:43 UT. White contours are the microwave maps, and the background images are the Hα

center-line image in the left panel (with a larger field of view) and the blue-wing images in the right panels. Microwaves are emitted via the synchrotron mechanism by high-energy electrons gyrating about the magnetic field and are sensitive to a wide range of magnetic field according to frequency (Bastian et al. 1998). In the 2002 September 9 event, the microwave sources show the expected morphological variation with frequency. The low-frequency (2.9 GHz) microwave source appears to encompass all three Hα blue-wing ribbons and extends to the northern and western parts of the active region, which implies the presence of a large arcade-like structure running north-south alongside the umbra. This, in turn, explains why a number of Hα ribbons at the line center are found in those regions. These ribbons must also be energetically connected to the primary energy release site (presumably located close to the hard X-ray source), but energy deposition to these ribbons appears much weaker and only shows up in the Hα center line because it is much more
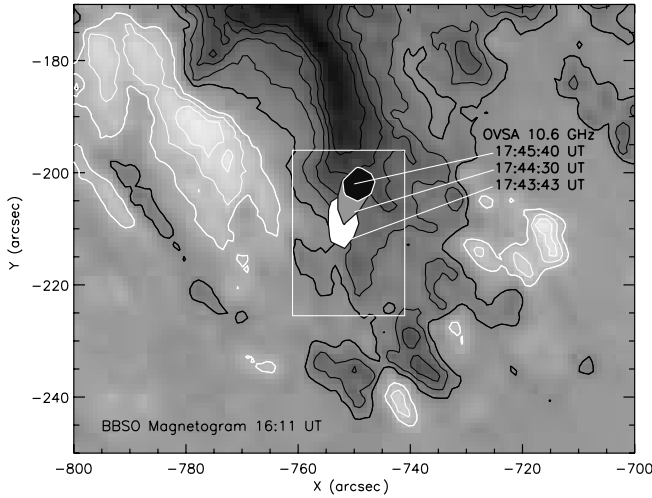
FIG. 5.—Time-dependent change of the locations of the 10.6 GHz source. The white, gray, and black polygons shown within the white box are the areas of the microwave source above 90% of the maximum intensity at each denoted time. The background image is the BBSO longitudinal magnetogram with white (black) contours representing the positive (negative) longitudinal magnetic field strengths starting from ±150 G and increasing (decreasing) in intervals of 150 G. The white rectangular box in the middle indicates the area used for the display in Fig. 6.

easily excited. The 6.1 GHz source covers both kernels $a1$ and $a2$, with some tail still extending along the north arcade, and at 14 GHz the source is concentrated at one of the conjugate kernels, $a2$, due to its higher field strength. Such morphological variation with frequency allows us to trace the region of energetic electrons. In this case, the ribbon $a2$ appears to be a region of intense electron precipitation.

In Figure 5 we show the 10.6 GHz source at three consecutive times to show its motion with time relative to the magnetic neutral line. The white, gray, and black polygons lying within the white box are the areas of the microwave source above 90% of the maximum intensity at each denoted time. The background image is the BBSO longitudinal magnetogram taken at a nearby

time (16:11 UT) superposed by white (black) contours representing the positive (negative) longitudinal magnetic field starting from ±150 G and increasing (decreasing) in intervals of 150 G. The white rectangular box in the middle indicates the area chosen to display the subtle motion in more detail in Figure 6. In this figure, the 10.6 GHz source moves from the periphery of the sunspot toward the umbral center. We show in Figure 6 that this is also true of the motion of the Hα ribbon $a2$ and thus conclude that the motion of the $a2$ ribbon is associated with the precipitation of high-energy electrons.

As to whether the microwave source moved perpendicular to the magnetic neutral line, Figure 5 shows that it certainly moved away from the nearest local magnetic neutral line. Its directivity relative to the nearby neutral line could, however, be debatable because this active region consists of a round sunspot surrounded by well-confined parasitic fields, so the neutral lines (more precisely, the field-free region between two different polarities) are highly distorted around the sunspot. Note also that the active region is located close to the eastern limb, making the round sunspot look elongated along the north-south direction and furthermore creating an apparent polarity reversal in the eastern side of the sunspot. As a result the directivity of the motion relative to the neutral line is ambiguous. We believe that a more important and meaningful criterion in this situation is the direction of the magnetic field gradient in the sunspot. Since the field in the umbral center will reach a higher coronal height than those lying more distant from the center, the path of the microwave source along the local gradient of the sunspot field indicates that the reconnection proceeded upward in the corona. This is consistent with what we expect from the ribbon motion perpendicular to the magnetic neutral line.

4. ANALYSIS

In this section we analyze the observational data to derive the physical parameters associated with the magnetic reconnection. Prior to making such an analysis, we justify our approach in § 4.1 and give a definition of the ribbon velocity in § 4.2. We then present the analysis result of the magnetic field in § 4.3 and that of electrons in § 4.4.
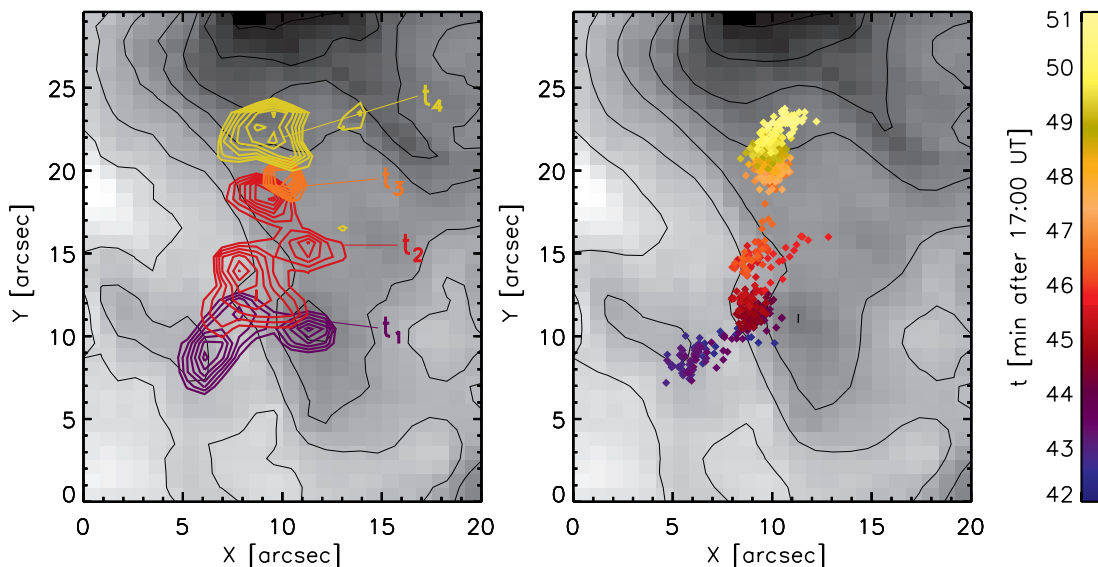

FIG. 6.—Location and area of the Hα blue-wing ribbon overlaid on a Michelson Doppler Imager (MDI) magnetogram (*gray scale*). *Left*: Emission contours marking the areas of the ribbon at selected times. *Right*: Filled circles marking the locations of the center of mass of the ribbon on the magnetogram. The color scale for time is shown at the far right; t_1–t_4 refer to 17:43:26, 45:22, 46:45, and 49:22 UT, respectively, which are commonly used in the rest of figures.

4.1. *Justification*

As Figure 5 shows, the active region consists of a round sunspot surrounded by several isolated parasitic poles, and the neutral line is highly distorted, which is far from a simple two-dimensional (2D) symmetry. However, the ribbon itself is quite confined and, by its short length, can be regarded as a thin 2D slice of a three-dimensional (3D) magnetic field. We thus consider the ribbon size alone making it conform to the 2D geometry, regardless of the distorted nature of the neutral line nearby. The next criterion is that the flare geometry should be not only 2D but a specific 2D lying perpendicular to the magnetic neutral line. The highly distorted neutral line in this event makes it hard to judge against this criterion. We, however, argued in § 3.3 that the path of the radio source is along the local gradient of the sunspot fields, and it can be indicative of the reconnection proceeding upward in agreement with the FP82 model. This magnetic configuration differs from the event studied by Grigis & Benz (2005), in which the X-ray footpoint motion was found parallel to the neutral line and could be attributed to the reconnection proceeding along the magnetic arcade. In the present case it is hard to believe that an arcade extends from the sunspot penumbra to the umbral center. The last thing that we cannot clarify is the presence of the counter–ribbon motion in the other polarity. The main difficulty lies in that these field lines stem from a well-confined parasitic pole, and the motion within that narrow region is not clearly traceable. Since this is an observational limitation, we leave this question open and proceed to analyze only the well-observed part of the reconnecting loop, i.e., the ribbon $a2$ only.

4.2. *Velocity Measurement*

Determining the ribbon speed is another key step in this analysis, which is not necessarily obvious because the actual ribbons appear in a more complicated form than in the standard 2D model. A simple way to determine the ribbon motion is to pick a typical point within the ribbon, for instance, either the point of highest intensity or an average point of the outer ribbon edge in the direction of the separating motion. Asai et al. (2004a) focused on the leading edge of the expanding ribbon, using the motion perpendicular to the magnetic neutral line to be consistent with the standard theory, while Jing et al. (2005) used an algorithm to compute a vector average of the velocities determined from incremental change of area per unit time.

To convince ourselves which definition is more appropriate in the present case, we examine the blue-wing ribbon morphology as shown in Figure 6 (*left*). It shows ribbon $a2$ at four selected times as color contours. The area is set by the lowest contour corresponding to 30% of the maximum intensity at each time. The size and morphology of the ribbon changes with time. If we choose a particular point on the leading edge of the ribbon, the resulting velocity would involve not only the mean average motion of the ribbon but the peculiar velocities due to the time-dependent ribbon boundary. Since this study assumes that the ribbon can have a finite area independent of the mean velocity, we do not want any peculiar velocities due to expansion or shrinking of the area to be confused with the mean velocity. In this case, the so-called center-of-mass location would be a more relevant and less ambiguous quantity, namely, $X_c \equiv \sum X_i I_i / \sum I_i$, where I_i is the Hα blue-wing intensity at pixel location X_i. Figure 6 (*right*) shows the locations of the centers of mass at multiple times as colored filled circles. Points concentrated within a narrow region signify that the ribbon is more or less stationary in that region; gaps between groups of con-
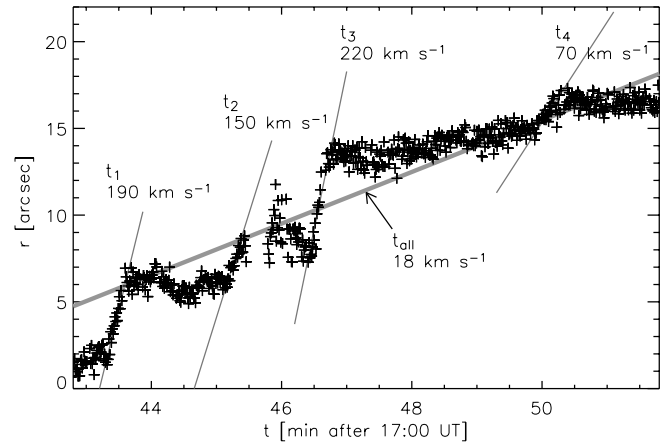

Fig. 7.—One-dimensional distance of the center of mass of the ribbon (*plus signs*) as a function of time. Five time intervals during which the distance rapidly increases are marked with solid guide lines along with the inferred speeds. Another fit to the overall motion in the entire period is also shown as a thick gray line for comparison.

centrated points correspond to the locations where the ribbon speeds up under the enhanced magnetic flux reconnection.

The time-stamped point distribution in Figure 6 (*right*) suggests that the ribbon motion is not uniform but rather stepwise. This is more clearly seen in Figure 7, where the location of the ribbon (*plus signs*) is shown as a function of time together with the solid guide lines showing the speed determined at selected time intervals. The first stepwise motion, for instance, occurs around ∼17:43:30 UT at which time the ribbon is advancing about ∼5″ in ∼20 s achieving the speed ∼160 km s^{-1} (see the solid guide lines indicating the speed). Other stepwise motions also incur high velocities ranging from ∼60 to ∼220 km s^{-1}, which are much higher than the typically reported ribbon velocity, a few tens of kilometers per second (Jing et al. 2005). In order to check why such an enormously different result is obtained in the present case, we made another fit to the average motion over the whole period of the flare activity. If we count the distance after 17:43:30 UT, the total distance traveled is ∼10″ in ∼7 minutes, and the overall speed is only ∼18 km s^{-1} (shown by the thick guide line marked as t_{all}), in agreement with the above-mentioned typical speed. An issue is then whether we should take, for the representative ribbon speed, the overall average motion or the intermittent motion. From the physical point of view, we show that these stepwise motions do agree, in timing, with the multiple peaks of hard X-rays, and they are therefore scientifically significant. Technically, we also see no reason to doubt those momentarily high speeds. There is, of course, a concern that apparent fast image fluctuation may arise from either time-dependent seeing or error in alignment. But such fluctuations appear at much shorter timescales (≤1 s), whereas the motions marked in Figure 7 show an obvious trend persisting over 10–20 measurements (≥10 s). We hence propose that the ribbon motion is intrinsically that fast and highly intermittent by nature.

4.3. *Magnetic Energy Release*

Figure 8 shows all the quantities as functions of time. The top three panels show the measured parameters (B_f, v_f, and A_f) and the bottom three the derived quantities (E, $\dot{\Phi}_B$, and $\mathcal{E}_B$). The gray histogram shown in the background is the *RHESSI* count rates at 25–50 keV for comparison. The magnetic field shown in the top panel is read from the BBSO magnetogram (Fig. 5) at the
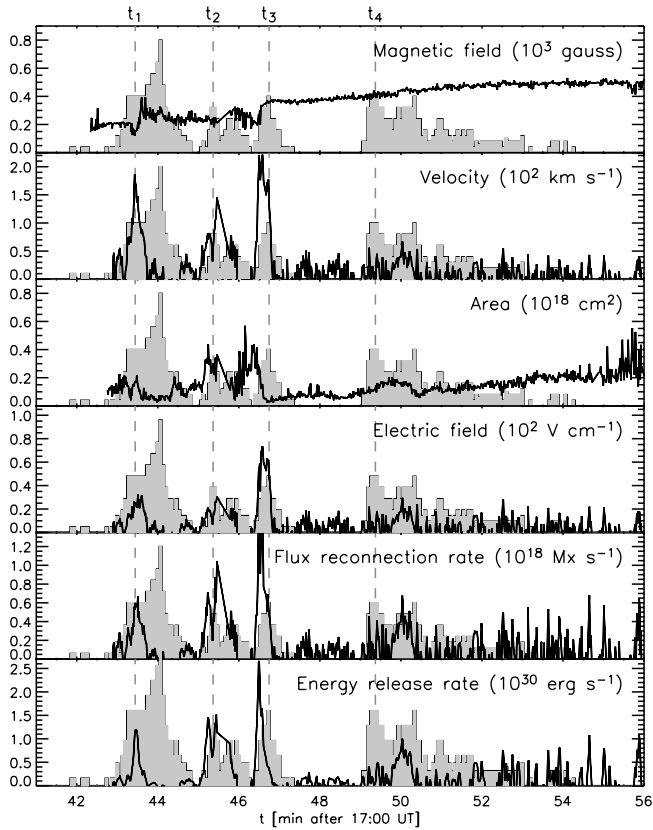
Fig. 8.—Physical parameters of the magnetic reconnection as functions of time in the 2002 September 9 flare. The top three panels show observed parameters: local magnetic field strength, ribbon velocity, and area. The bottom three panels show derived quantities: electric field, flux change rate, and energy release rate. The gray histogram in each panel shows the *RHESSI* count rate at 25–50 keV for reference.

location of the center of mass of the *a*2 ribbon at each time. However, the flux change rate and energy release rate are calculated by integrating the relevant quantities over the ribbon area.

At a glance, we see that most of the quantities are episodic with the hard X-ray count rates, except the magnetic field. This means that the good time correlation between the electric field and the X-ray light curve is due to the velocity rather than the inhomogeneous magnetic field. The flux change rate and energy release rate also show episodic variations except that for these quantities the change in area also contributes to the temporal variations. These results are in agreement with previous studies showing correlations of X-ray light curves with velocity (Fletcher & Hudson 2001), electric field (Qiu et al. 2002), and flux change rate (Jing et al. 2005). A new result is that the area measured in the blue wing of Hα also shows an episodic variation and thus plays a role in the time variation of the magnetic energy release.

The maximum electric field reads ~74 V cm^{-1}. This might be considered unusually high for this M2.3 class flare when compared with that typically found ($\leq$10 V cm^{-1}) in the literature, including stronger X-class flares (Jing et al. 2005; Krucker et al. 2005). We believe that two things could be involved in the high electric field strength. One is that we obtained an unusually high velocity. The maximum speed is as high as ~220 km s^{-1}, whereas the ribbon speed found in other studies is typically around a few tens of kilometers per second (Jing et al. 2005). This is partly because the ribbon motion is s highly intermittent; it moves quickly and stops for a while before resuming its motion, which

could have been greatly underestimated if a lower cadence were used. The other is that the electric field is not necessarily a measure for the soft X-ray flux, and therefore a small flare can have a high electric field. This point is further discussed in § 5. The maximum flux reconnection rate reaches ~1.3 × 10^{18} Mx s^{-1}, which is modest when compared with the previously found values: $(0.5–2) \times 10^{18}$ Mx s^{-1} by Jing et al. (2005). This again implies that the high velocity was the main factor for the high electric field.

Finally, the maximum energy release rate in Figure 8 is ~2.6 × 10^{30} ergs s^{-1}, to be compared with commonly cited total flare energies, e.g., 10^{32}–10^{33} ergs in 10^2–10^3 s for the largest flares (Lin et al. 2002). Upon integration over the full period of the flare, the total amount of magnetic energy released comes to ~1.0 × 10^{32} ergs, which is rather close to the commonly cited values for the most powerful flares, 10^{32}–10^{33} ergs (Lin et al. 2002). Our result is certainly larger than $\dot{\mathcal{E}}_B \leq 10^{29}$ ergs s^{-1} that Krucker et al. (2005) found for an X10 flare, as a little surprise. We employed somewhat different assumptions from those in Krucker et al. (2005) about the dimension of the RCS. However, it appears that the quantitative difference mainly comes from the field strength and ribbon velocity rather than from the dimension of the RCS.

4.4. *Comparison with Electron Energy*

The energy of electrons emitting X-rays can be determined by inverting the observed X-ray spectrum to obtain the electron energy distribution. In principle, this inversion can be made for any type of X-ray spectrum and any time, so long as there is a sufficient number of photons in a wide energy range (e.g., as in the case of the X10 flare studied by Krucker et al. 2005). For this event, the X-ray spectrum is so soft that we could not determine the spectral morphology in detail. We thus attempt the inversion only in some selected intervals of highest intensity under the assumption of a single power-law photon flux spectrum, namely, $F(\epsilon) = \mathcal{A}\epsilon^{-\gamma}$ in units of photons keV^{-1} cm^{-2} s^{-1}. In this case, Brown's formula (Brown 1971) gives an expression for the electron deposition rate per energy, $Q(E)$, in units of electrons keV^{-1} s^{-1}. For our purpose, we calculate the total electron energy deposition rate, which can be defined as

$$\dot{\mathcal{E}}_{\rm el} = \int_{E_0}^{\infty} Q(E)E\,dE \approx 6.74 \times 10^{24} \mathcal{A}\gamma(\gamma-1)B\left(\gamma - \frac{1}{2}, \frac{1}{2}\right) E_0^{-\gamma+1},$$

(6)

in units of ergs per second. Here B is the beta function, and E is electron energy in keV.

TABLE 1

Electron Energy Deposition Rate versus Magnetic Energy Release Rate

Period (UT) (1)	γ (2)	$\mathcal{A}$[a] (3)	E_0 (keV) (4)	$\dot{\mathcal{E}}_e$ (ergs s^{-1}) (5)	$\dot{\mathcal{E}}_B$ (ergs s^{-1}) (6)
43:43–44:15...............	5.6	100	10	1.4 × 10^{29}	1.2 × 10^{30}
44;15–44:55...............	7.0	200	10	4.0 × 10^{29}	1.5 × 10^{30}
46:30–47:10...............	7.2	200	10	5.5 × 10^{29}	2.6 × 10^{30}
49:05–49:45...............	7.3	70	13	5.6 × 10^{29}	6.7 × 10^{29}
49:50–50:38...............	7.4	80	13	5.7 × 10^{29}	1.1 × 10^{30}

[a] In units of photons keV^{-1} cm^{-2} s^{-1}.

We list the results in Table 1. Column (1) shows the time intervals chosen (following those of Ji et al. 2004), and columns (2) and (3) list the values of $\mathcal{A}$ and γ, respectively, read from Figure 5 of Ji et al. (2004) for our assumed E_0 (col. [4]). Note that this is a rough estimate because the spectrum is too soft to identify the lower and higher energy cutoff or single/double power law to which the resulting energy is sensitive. Considering the limitations involved in each estimate, the agreement is satisfactory in that the electron energy deposition rate lies within 10%–80% of the magnetic energy release rate. A subtle point to note is that our derived magnetic energy release rate correlates with the electron energy (listed in Table 1) better than the observed hard X-ray 25–50 keV flux (shown in Fig. 6). This results because the *RHESSI* X-ray spectrum becomes softer with time (see Table 1), and a larger number of electrons should be involved in a softer photon spectrum to produce a comparable radiative output (see eq. [5]).

5. DISCUSSION

The flare kernel motion during the 2002 September 9 flare was observed with an unusually high time cadence in off-band Hα and with a moderate resolution in microwaves, which motivated us to study the magnetic energy release process of this flare in detail. The previous approaches for the magnetic energy release (Isobe et al. 2002, 2005; Asai et al. 2002, 2004a; Krucker et al. 2005) differ slightly from each other in terms of the assumptions made to link the photospheric parameters to the coronal counterparts, to which the accuracy of the result would also be subject. In this regard we briefly discuss how our approximation differs from others and comment on the most plausible physical mechanism to explain our result.

In the present approach, our emphasis has been on considering the kernel area as an important factor in the magnitude of the energy release rate. A key assumption in linking this to the coronal RCS area is that the RCS maintains a constant aspect ratio or, equivalently, reconnection rate, $M \approx 0.1$. This specific value is based on an existing numerical experiment of the Petschek model (Yan et al. 1992) and also consistent with the approximation made for the theoretical expression of the energy release rate (see Appendix). Similarly, Asai et al. (2004a) also introduced a constant factor to relate the photospheric field to the coronal field. A difference is that our approach takes into account the time-dependent variation of the RCS area as an important factor in the energetics and dynamics of the magnetic reconnection (see below). Krucker et al. (2005) followed the Asai et al. approach to find an energy release rate lower than ours by 1 order of magnitude, which seems to be largely due to differences in ribbon velocity rather than to the dimension of the RCS. As mentioned in §§ 2 and 4, we believe that the unknown filling factor has not greatly affected our estimate for the energy release rate. It is the high time cadence that allowed us to catch the episodically high speed of ribbon motion and thus derive a correspondingly high energy release rate. On the other hand, Isobe et al. (2005) aimed at determining the reconnection rate, M, while the dimension of the RCS is taken from that of the flare arcade (see also Yokoyama et al. [2001] and Lin et al. [2002] for an alternative determination of M). Certainly the magnetic reconnection rate can vary with time, and we previously thought that comparison of the magnetic energy release with the electron energy deposition rate could be used to determine the temporal variation of the reconnection rate. However, in view of the level of approximations made in both the magnetic and the electron energy estimates, such analysis appears to remain premature.

As shown in Table 1, the total electron energy need not exactly correlate with the photon flux at a given energy interval because the spectral index and cutoff energies come into play. A more accurate determination of the total electron energy than in the present study will be necessary in order to infer the time-dependent reconnection rate in this way.

In some other studies, electric field or flux reconnection rate are compared with X-ray or microwave light curves. Undoubtedly, a good time correlation between them would argue that the magnetic reconnection is involved in each episode of particle acceleration. However, it remains questionable as to whether a higher electric field should result in a more powerful flare. Theoretically, electric field is a measure of acceleration efficiency per particle, whereas the flare strength, given in terms of soft X-ray flux, depends on the integral number of electrons in the entire energy range. Observationally, a correlation between electric field strength and flare strength exists, but it is weak (Jing et al. 2005). Strong electric fields are found in an M-class (present study) or even a C-class flare (Qiu et al. 2002) and may exceed those found in X-class flares (Jing et al. 2005). It is likely, in the perspective of equation (5), that the temporal correlation of the electric field with X-ray light curves may imply that the electric field effectively controls the temporal behavior of the magnetic energy release rate rather than its integral magnitude. A statistical study of the total magnetic energy released in a range of flares is therefore worthy of future effort.

Finally, we ask ourselves a more fundamental question in understanding solar flare magnetic reconnections: which parameter most strongly governs the flux reconnection rate, the incoming velocity or the magnetic field strength? Asai et al. (2002, 2004a) addressed, in detail, a similar issue—when or where the strong energy release occurs. They suggested an essential role for magnetic field strength, for both the reconnection rate and the energy release rate, because hard X-ray ribbons are often found in those parts of Hα ribbons with stronger magnetic field. Unlike their events, the ribbon in the 2002 September 9 event is not extended in parallel lines but rather forms a single, confined area, so we cannot provide answers to the spatial problem: which areas of the ribbon should be brighter than the others. The time-dependent part can, however, be discussed with the present result. First, looking at the result of Krucker et al. (2005), we find that not the magnetic field strength but rather the ribbon velocity correlates with the peaks in the X-ray light curves (although only a couple of points are used to define each peak). We here obtained the same result as Krucker et al., but with higher cadence, that the magnetic energy release appears highly intermittent in time, and this intermittence comes from the velocity rather than magnetic field variation.

We further showed that not only the velocity but also the kernel area shows episodic variation. Which parameter initially triggers the reconnection is an important issue that is still in theoretical debate. The FP82 model merely predicts a proportion between electric field and inflow speed as a cause-effect relationship; i.e., whether the reconnection drives the inflow or vice versa remains unknown. In a theory developed for radio pulsations (Kliem et al. 2000), however, the RCS area can, at least, be involved in a self-organized evolution, in such a way that increase of current density and thus anomalous resistivity (Huba 1985) makes the RCS area expand, leading in turn to a decrease in current density. A series of such self-organized cycles would, in this view, produce the multiple peaks in X-ray/microwave light curves as observed. We thus propose that the episodic time variations of the ribbon speed and area, but not that of the magnetic

field, can be explained by this pulsating current sheet model (Kliem et al. 2000). The concept of the ribbon area as a dynamic quantity introduced in this paper therefore not only provides a way for determining the amount of energy release but also provides physical insight into the dynamical evolution of the RCS.

APPENDIX

COMPARISON OF THE INCOMING AND OUTGOING POYNTING FLUXES

In the geometry shown in Figure 1, the incoming Poynting flux is $S_x = E_i B_i = v_i B_i^2$. There can be an additional term associated with the sheared magnetic field B_i, which we, however, ignore for simplicity. Likewise, the outgoing Poynting flux is $S_z = E_o B_o = v_o B_o^2$. The ratio of the energy flux outgoing through A_z to that incoming through A_x is then

$$\frac{|S_z A_z|}{|S_x A_x|} = \left|\frac{A_z v_o B_o^2}{A_x v_i B_i^2}\right| = \left|\frac{A_z}{A_x}\right|\left|\frac{B_o}{B_i}\right| = M^2. \tag{A1}$$

This ratio is much smaller than unity when $M \approx 0.1$ as assumed. We can therefore conclude that the energy flux going out through A_z is much smaller than the incoming flux through A_x, and equation (1) becomes an approximate expression for the energy release rate in the RCS when $M \ll 1$. Otherwise, if the reconnection is less efficient ($M \sim 1$), the right-hand side of equation (1) will have extra terms and the energy release rate is reduced as a result, which is, however, not regarded as the case for solar flares. It can easily be shown that the above relationship remains approximately valid in a more realistic case in which both $\boldsymbol{B}_i$ and $\boldsymbol{B}_o$ have sheared magnetic field components, i.e., y-components.

REFERENCES

Asai, A., Masuda, S., Yokoyama, T., Shimojo, M., Isobe, H., Kurokawa, H., & Shibata, K. 2002, ApJ, 578, L91
Asai, A., Yokoyama, T., Shimojo, M., Masuda, S., Kurokawa, H., & Shibata, K. 2004a, ApJ, 611, 557
Asai, A., Yokoyama, T., Shimojo, M., & Shibata, K. 2004b, ApJ, 605, L77
Bastian, T. S., Benz, A. O., & Gary, D. E. 1998, ARA&A, 36, 131
Brown, J. C. 1971, Sol. Phys., 18, 489
Canfield, R. C., Gunkler, T. A., & Ricchiazzi, P. J. 1984, ApJ, 282, 296
Dennis, B. R. 1988, Sol. Phys., 118, 49
Dennis, B. R., Veronig, A., Schwartz, R. A., Sui, L., Tolbert, A. K., & Zarro, D. M. 2003, Adv. Space Res., 32, 2459
Fletcher, L., & Hudson, H. 2001, Sol. Phys., 204, 69
———. 2002, Sol. Phys., 210, 307
Forbes, T. G., & Priest, E. R. 1982, Planet. Space Sci., 30, 1183 (FP82)
Grigis, P. C., & Benz, A. O. 2005, ApJ, 625, L143
Huba, J. D. 1985, in IAU Symp. 107, Unstable Current Systems and Plasma Instability Astrophysics, ed. M. R. Kundu & G. D. Holman (Dordrecht: Reidel), 315
Isobe, H., Takasaki, H., & Shibata, K. 2005, ApJ, 632, 1184
Isobe, H., Yokoyama, T., Shimojo, M., Morimoto, T., Kozu, H., Eto, S., Narukage, N., & Shibata, K. 2002, ApJ, 566, 528

Ji, H. S., Wang, H., Schmahl, E. J., Qiu, J., & Zhang, Y. A. 2004, ApJ, 605, 938
Jing, J., Qiu, J., Lin, J., Qu, M., Xu, Y., & Wang, H. 2005, ApJ, 620, 1085
Kliem, B., Karlický, M., & Benz, A. O. 2000, A&A, 360, 715
Krucker, S., Fivian, M. D., & Lin, R. P. 2005, Adv. Space Res., 35, 1707
Lin, R. P., et al. 2002, Sol. Phys., 210, 3
Litvinenko, Y. E. 2000, Sol. Phys., 194, 327
Noglik, J. B., Walsh, R. W., & Ireland, J. 2005, A&A, 441, 353
Petschek, H. E. 1964, in The Physics of Solar Flares, ed. W. N. Hess (NASA SP-50; Washington: NASA), 425
Priest, E. R. 1982, Solar Magnetohydrodynamics (Dordrecht: Reidel)
Priest, E. R., & Forbes, T. G. 2000, Magnetic Reconnection: MHD Theory and Applications (Cambridge: Cambridge Univ. Press)
———. 2002, A&A Rev., 10, 313
Qiu, J., Lee, J., Gary, D. E., & Wang, H. 2002, ApJ, 565, 1335
Tang, F. 1983, Sol. Phys., 83, 15
Yan, M., Lee, L. C., & Priest, E. R. 1992, J. Geophys. Res., 97, 8277
Yokoyama, T., Akita, K., Morimoto, T., Inoue, K., & Newmark, J. 2001, ApJ, 546, L69